

CrystEngComm

Accepted Manuscript



This is an *Accepted Manuscript*, which has been through the Royal Society of Chemistry peer review process and has been accepted for publication.

Accepted Manuscripts are published online shortly after acceptance, before technical editing, formatting and proof reading. Using this free service, authors can make their results available to the community, in citable form, before we publish the edited article. We will replace this *Accepted Manuscript* with the edited and formatted *Advance Article* as soon as it is available.

You can find more information about *Accepted Manuscripts* in the [Information for Authors](#).

Please note that technical editing may introduce minor changes to the text and/or graphics, which may alter content. The journal's standard [Terms & Conditions](#) and the [Ethical guidelines](#) still apply. In no event shall the Royal Society of Chemistry be held responsible for any errors or omissions in this *Accepted Manuscript* or any consequences arising from the use of any information it contains.

Chemically derived CuO/In₂O₃ based nanocomposite for diode applications

**G. Mohan Kumar^{a*}, P. Ilanchezhian^a, A. Madhan Kumar^b, T. S. Shabi^c,
S. Tamil Selvan^d, S. Suresh^e, Sh. U. Yuldashev^a and T. W. Kang^{a*}**

^aQuantum-Functional Semiconductor Research Center,
Dongguk University, Seoul, Republic of Korea.

^bCenter of Research Excellence in Corrosion,
King Fahd University of Petroleum & Minerals, Kingdom of Saudi Arabia.

^cDepartment of Polymer Science and Engineering
Zhejiang University, Hangzhou, China.

^dAdvanced Materials Processing and Analysis Center,
NanoScience Technology Center, Materials Science Engineering,
University of Central Florida, Orlando, USA.

^eGT-CNRS-UMI Lab, Georgia Institute of Technology,
2-3, rue Marconi, Metz, France.

Fax: +82-2-2278-4519; Tel: +82-10-4896-1777

Email: selvi1382@gmail.com, twkang@dongguk.edu

Abstract:

Nowadays, oxide based semiconducting nanostructures are widely regarded as one of the most essential elements of modern semiconductor industries and for a number of advanced technological functions in electronics and optoelectronic platform. In this regard, a CuO based nanocomposite was synthesized through a facile surfactant free wet chemical strategy and their potential for photoelectronic applications has been demonstrated. The nature of composite phase and their other structural characteristics were studied in detail using Raman and X-ray photoelectron spectroscopic tools. The particulate characteristics of the composite were inferred using transmission electron microscopic measurements. The room-temperature luminescence measurements revealed the optical activity of composite to spread across the red and near-infrared region of the electromagnetic spectrum through corresponding transitions. The optoelectronic capabilities of the processed composite were investigated through fabricating a CuO composite/ZnO nanowire made p-n heterostructure and studying their associated current-voltage (I-V) characteristics under photon illumination. The nature of charge carriers, flat band potential, charge transfer resistance and carrier density were also studied individually and collectively for each component comprising the heterostructures through Mott-Schottky and Nyquist type impedance plots.

Introduction:

Semiconducting oxide nanostructures are considered to be one of the most vital candidates for a number of technological functions, owing to their low-cost manufacturing techniques and improved physicochemical characteristics [1-6]. The primary interest beneath such material systems could be attributed to their exceptional environmental stability and diversified material processing strategies reported so far [7-9]. In the last few years, significant advancements have been made in the synthesis/studies of a large array of oxide systems in one, two and three dimensional configurations, which in parallel have also fuelled their application in sensors, memory devices, thin-film transistors, solar cells, etc. [10-14]. However, a fundamental understanding on the optical and electrical properties of such oxide nanomaterials seems to be highly essential from commercial perspectives, for the visualization/demonstration of improved device functionalities. Recently, transition metal oxides (TMO) have started to gather special interest in organic and organic-inorganic hybrid electronic devices (as active/functional layers, with unique and exceptional charge injection and extraction properties), to assist with the realization of their high performance [14-18].

Among the TMO family, cupric oxide (CuO - 1.2 to 1.9 eV) and cuprous oxide (Cu_2O - 2.2 eV) are of recent specific interest for photonic applications, due to their superior solar absorbency power, lower thermal emittance and other interesting photoelectronic properties [19-22]. This class of p-type semiconductor is widely believed to possess the ability to replace traditional semiconductors and encourage the fabrication of cost-effective solar cells. Their non-toxic nature and unique physicochemical properties are of added interest, as they could be tailored in accordance with the application of study [23, 25]. So, from such viewpoints a noteworthy attempt has been made in the present case to tailor synthesize a nanocomposite form of CuO for low cost electronic applications. To attain the desired

composite, indium oxide (In_2O_3) was opted as the viable candidate for their blend with CuO. This selection was actually made after considering their superior electrical properties and optical transparency over the visible regime [25-27]. We also believe that such associations i.e. brewing a wide band gap semiconductor like In_2O_3 with a narrow band gap CuO could open up a multitude of applications in electronics and optoelectronics forum, especially with the realization of terahertz and photonic devices [28-32]. However, to preserve certain intrinsic functions of CuO such as its p-type conductivity and band gap, its corresponding composition was held to be four fifths in the processed composite blend (explained in the experimental section).

In the present context, this article can be divided into two parts, with the first part addressing the issues related to the fabrication and characterization of a new and intriguing composite material (composed of CuO- In_2O_3), through effective solution synthesis. Here, the adopted experimental techniques were found to be relatively simple in this regard and ensured the successful formation of nanocomposites. The processed composite material is here after referred as Cu-In-O. The transmission electron microscopic (TEM/HRTEM) imaging on Cu-In-O revealed the existence of distinct characteristics corresponding to that of CuO and In_2O_3 . The other structural, optical and electrochemical characteristics of Cu-In-O were also collectively examined to determine their potential for electronic applications. In the second part, the solution processed p-type Cu-In-O was integrated with the n-type zinc oxide (ZnO), for the realization of p-n diode architectures. ZnO was actually preferred in form of nanowires (hydrothermally grown) in such architectures, as they are unique materials that could assist with the generation of direct pathways for efficient charge transferring [33-36]. The current-voltage (I-V) characteristics established across the fabricated heterostructures demonstrated an improved photocurrent to flow across their integrated structures, with

significantly reduced reverse leakages. The results obtained through the present investigations signify the importance of processing novel materials and effective architectures for low cost electronic applications.

Experiment:

Materials: All the chemicals used in the experiments were of analytical grade and used thereafter. Copper acetate, indium acetate, zinc acetate, zinc nitrate and potassium hydroxide (KOH) pellets were procured from Sigma-Aldrich. The ITO substrates (15Ω) used in the fabrication of working electrodes were pre-cleaned in acetone, ethanol and deionized (DI) water.

Synthesis of Cu-In-O nanocrystals: Copper acetate and indium acetate precursors (in a weight ratio of 4:1) were initially dissolved in 100 ml of DI water and continuously stirred for 24 h to ensure the homogeneity between the metallic precursors. The obtained mixture was then precipitated using 15 ml of 10 M KOH solution. Here, the addition of KOH was made in drops until it was ensured that the precipitation ceased. The resulting suspension was further subjected to ultrasonic treatment for a period of 30 min to improve the pyrolytic reactions of H^+ and OH^- ions. Generally, such treatments are believed to help with the successful formation of hydroxyl groups *via* enhancing the activity of corresponding base agent. After ageing the resulting precipitates for another 24 h, the yield was harvested through washing with DI water and ethanol (to remove the possible ionic impurities). The final products were dried at room temperature and calcined at $800 \text{ }^\circ\text{C}$ for 2 h before further studies.

Characterization: The crystal structure of the calcined samples was analysed at a scan rate of $0.02^\circ \text{ s}^{-1}$ in an X-ray diffractometer (XRD-RINT 2000) using Cu-K α radiation ($\lambda = 0.154 \text{ nm}$), over a 2θ range of $20\text{-}65^\circ$. The room-temperature Raman measurements were carried

out using a Micro Confocal Raman spectrophotometer, with an excitation wavelength of 514.5 nm. The morphology and dimensions of the obtained products were obtained using a transmission electron microscope (JEOL TEM-2100F). The X-ray photoelectron spectroscopic measurements were carried out using a PHI 660 XPS spectrometer (using Al $K\alpha$ radiation (1486.6 eV) as the excitation source). The absorbance spectrum was recorded using a Cary UV/VIS/NIR spectrophotometer, while the emission characteristics were carried out under an excitation wavelength of 488 nm. The morphological distribution of the nanocrystalline products and the heterostructure interface were examined using an atomic force microscope, Shimadzu SFT 3500 and scanning electron microscopes, Hitachi (S4800) and JEOL JSM 6460LV. The room-temperature current-voltage (I-V) characteristics were studied using a Keithley 617 semiconductor parameter analyzer, with a 140 W Xenon lamp. The electrochemical studies were carried out using a simple three-electrode system, where the drop casted films acted as the working electrode, while Ag/AgCl/KCl and Pt sheet served as the reference and counter electrodes, respectively.

Results and discussion:

The structural characteristics of Cu-In-O composites were initially studied using the aid of X-ray diffraction (XRD) spectrum shown in Figure 1a. Here, the recorded diffractogram reveals the occurrence of distinct signatures that corresponds to that of CuO and In_2O_3 , respectively. The peaks located at 35.39 and 38.58° are the prominent features that characterize the (002) and (111) crystal planes of monoclinic CuO and are also in consistent with the JCPDS file (48-1548). Similarly, the In_2O_3 characteristics could be inferred through the diffraction corresponding to their (222) planes at $\approx 30^\circ$. Eventually, the possibility for existence of any $\text{Cu}(\text{OH})_2$ or Cu_2O phases among the processed composite was ruled out through the absence of their corresponding diffraction characteristics [24].

The structural characteristics of Cu-In-O were additionally studied using Raman spectroscopy. This branch of spectroscopy is widely believed to possess the potential to evaluate the nature of distortions developed in a crystal's local translational symmetry that could be induced on doping or substitution. Figure 1b shows the room-temperature Raman spectrum of Cu-In-O, which depicts the subjected laser radiation to activate vibrations at 123.40, 281.44, 324.88, 554.49, 612.59 and 1093.25 cm^{-1} , respectively. Here, apart from the first vibration at 123 cm^{-1} the remaining vibrations could be correlated with that of the monoclinic phased CuO (where each Cu ion is located in a plane formed by two almost equidistant pairs of oxygen) [37]. CuO (C_{2h6} space group) in general is made up of two molecules per unit cell, with three acoustic modes, six IR active modes and three Raman active modes, correspondingly [38]. The vibrations at 281.44 cm^{-1} corresponds to the A_g mode in CuO and is believed to result from the vibration of O atoms. Similarly, the vibrations at 324.88 and 612.59 cm^{-1} could be attributed to the B_g modes in CuO. These vibrations are also believed to originate from the Cu-O stretching vibrations [39]. The appearance of a satellite structure at 554.49 cm^{-1} signifies the enhanced activity of IR modes in Cu-In-O systems that usually results from the loss of local inversion symmetry in CuO [40]. The two-phonon scattering ($2B_g$) of CuO was additionally verified in Cu-In-O, through the corresponding vibration at 1093 cm^{-1} . Likewise, the prevailing In_2O_3 characteristics in Cu-In-O was also inferred through the sharp peak centered at 123 cm^{-1} , which corresponds with that of the In-O vibration and arises from the InO_6 basic structural units [41].

The surface morphology of Cu-In-O composite was examined using electron microscopic tools. Figure 2a shows the results of transmission electron microscopic analysis, where the composite appears to be in form of granular agglomerates, with an average size of around 15-20 nm. The high-resolution TEM image shown in Figure 2b characterizes the mutual co-

existence of CuO and In₂O₃ characteristics in Cu-In-O, through the d spacing values corresponding to that of monoclinic phased CuO ($\{002\}$ and $\{111\}$) and cubic phased In₂O₃ ($\{222\}$). The observed interplanar lattice spacing values are well in agreement with our current XRD findings and other earlier reports [42, 43]. Despite the existence of two-different phases in Cu-In-O systems, TEM analysis hardly revealed any morphological difference between the same. The composition of Cu-In-O composites were additionally studied using an energy-dispersive X-ray spectrophotometer (EDS), which is commonly used as an effective analytical tool for the elemental analysis or chemical characterization of any material. In our case, the EDS spectrum that gives the elemental distribution of the constituent elements present in Cu-In-O is presented in Figure S1 (ESI). Here, the corresponding constituent elements namely Cu, In and O were confirmed on the basis of their weight ratio as 60, 12 and 28, respectively.

The nature of phases and valence state of transition metal ions present in Cu-In-O systems were additionally investigated using X-ray photoelectron spectroscopic (XPS) measurements. Figure 3a shows the Cu 2p core level spectrum that substantiates the 2+ state of Cu in Cu-In-O. This was actually affirmed through the 2p_{1/2} and 2p_{3/2} peak positions centered at 952.01 and 931.72 eV, respectively. Likewise, their relative positioning (≈ 20 eV) and occurrence of shake-up satellites at S₁ and S₂ characterizes the existence of CuO and rules out the possibility for any existence of Cu₂O in Cu-In-O [44, 45]. Figure 3b shows the In 3d core level spectrum that testifies the In₂O₃ characteristics and their valence state of 3+ in the composite system [46]. Figure 3c shows the O 1s core-level spectra (resolved through Gaussian curve-fitting procedure) demonstrating the occurrence of two distinct peaks centered at 528.32 and 530.70 eV, respectively. The former one on the lower binding energy

side implies the O^{2-} state (bound to the metal cations), while the latter one signifies the oxygen adsorbed over the surface of CuO and In_2O_3 , respectively [47, 48].

The optical absorbance characteristics of Cu-In-O composite were evaluated *via* recording the UV-vis absorbance spectrum for a colloidal dispersion that contained the processed nanocomposites (refer supplementary information). Figure 4a and its inset shows the UV-vis absorbance spectrum and the corresponding colloidal dispersion, which illustrates the competency of Cu-In-O to absorb light across the UV and visible spectrum, respectively. This behaviour also illustrates their potential as effective light absorbing materials in photodiode architectures (as it can directly influence the rate of charge carrier generation and improve their overall solar absorbency power).

The photo physical characteristics of Cu-In-O composites were investigated from the results of room-temperature photoluminescence measurements shown in Figure 4b. The spectrum reflects the remarkable emissivity of the material across the red and near-infrared regions (600-1100 nm) of the electromagnetic spectrum. To have a deeper understanding on the observed phenomenon, the obtained spectrum was subjected to Gaussian curve-fitting procedure. The resolved spectrum vividly describes the occurrence of three broad emissions centred at 1.53, 1.37 and 1.27 eV, respectively (denoted as a, b and c in Figure 4b). Here, the preceding one at 1.53 eV corresponds to the band gap of the material and could be attributed to the band-to-band transitions taking place in Cu-In-O. This energy gap value closely resembles with the indirect band gap of CuO, which is an intrinsic p-type semiconductor with an energy band gap of around 1.2-1.9 eV [49, 50]. Similarly, the origin of other two peaks could be advocated to the Cu-O or In-O related defect levels existing within the composite structure. Among such defects, the role of Cu related defects and especially their vacancies could have a limited influence on the observed emissions, as they are considered to be the

most stable form of defects that do not encourage the formation of new states within the band gap of the material [51]. So, the noted transitions in Cu-In-O could be reasoned with the oxygen vacancies or other antisite defects existing within the same [52, 53]. The oxygen vacancies present in the composite matrix could have readily interacted with the indium complexes and established certain trapped states within the bandgap of the material [54]. Such trapped states along with the co-existing In_2O_3 phases could have aided the observed transitions to spread across the far red region, through the multiple defect levels (oxygen and indium related) associated within their band gap [27, 55]. It is also noteworthy to mention here that by varying the composition between the two oxide phases in Cu-In-O, it is possible to engineer their bandgap and tune their emission characteristics between visible and near-infrared regions, correspondingly.

The potential of solution processed Cu-In-O composites for optoelectronic functions was investigated through fabricating vertical p-n heterostructures, composed of p-type Cu-In-O and n-type ZnO nanowires. The detailed procedure involved in the growth of ZnO nanowires and heterostructure fabrication has been provided in the supplementary information. The XRD pattern of the grown ZnO nanostructures and their corresponding cross sectional representations are shown in Figure S2 and S3, respectively (ESI). The distribution of the composite material across the heterostructure and the interface between Cu-In-O and ZnO was investigated through electron microscopic tools and the obtained results are shown in Figure S4 (ESI). Figure 5a shows the schematic representation of the fabricated photodiodes, whose photoelectric behaviour was studied under dark and illuminated conditions (using 140W Xenon lamp). The topological surface of the Cu-In-O/ZnO heterostructures was additionally examined through an atomic force microscope, whose corresponding three-dimensional representation is shown in Figure 5b. The microscopic results reveal the Cu-In-O

crystals to be well adhered as agglomerates on the surface of ZnO nanowires, forming a continuous interface. Figure 5c shows the excellent periodicity observed among the ZnO nanowires, with an average length of around 2 μm .

Figure 5d and its inset shows the corresponding results of current-voltage (I-V) characteristics that were measured at an applied potential of 0 \pm 10 V. The obtained results initially substantiate the realization of a p-n junction across the selected interface. And, this could be well understood through the significant variation in the asymmetric nature of current values and their nonlinear characteristics along the forward and reverse directions, respectively. Interestingly, the forward current was noted to improve across the diode from $1.10 \times 10^{-7} \text{ A cm}^{-2}$ to as high as $6.44 \times 10^{-7} \text{ A cm}^{-2}$ at 9 V under photon illumination, while the reverse leakage current remains almost same ($5.51 \times 10^{-8} \text{ A cm}^{-2}$ to as low as $5.78 \times 10^{-8} \text{ A cm}^{-2}$ at -10 V). The rectification ratio (forward to reverse current ratio) was found to improve 5 folds i.e. from 3 to 15 at 9 V, further complimenting the photoresponse behaviour from the corresponding diodes and signifying their semiconductor behaviour. The reduced leakages additionally signify a low level of interface related recombinations to take place across the processed heterostructures, possibly due to their energy level alignment (Figure S5, ESI).

Now, to assimilate the nature of charge transfer mechanism that takes place across the fabricated p-n heterostructures, the concept of built-in potential could be considered. Generally, it is quite common to visualize the realization of a built-in potential across any semiconducting p-n junctions [56, 57]. In our case, such potential could have decreased considerably across the heterostructures under forward bias conditions, thereby aiding the charge carriers to drift more readily. And, due to such behaviour the forward current seems to be much more remarkable in our case even under dark conditions. Similarly, the depletion width could have increased significantly under reverse bias conditions and hindered the easy

flow of charge carriers across the junctions (reason for much smaller reverse current). Furthermore, under illuminated conditions the net charge carriers could have increased considerably across the heterostructures and have further complimented with the improvement in built-in potential that augments the observed photoresponse behaviour. We also varied the thickness of Cu-In-O deposits on ZnO (through varying the number of drop cast cycles) to study their influence on the corresponding diode characteristics. The results are shown in Figure S6 and S7 and discussed accordingly in the supplementary information.

Electrochemical impedance spectroscopic (EIS) measurements were performed on pristine ZnO nanowires (D_1), Cu-In-O deposits (D_2) and Cu-In-O/ZnO made heterostructures (D_3), to assimilate the potential of the fabricated p-n junctions for electronic functions. The Mott-Schottky (MS) plot (representing the corresponding inverse square of capacitance against the applied potential) for the aforementioned working electrodes were initially established through a potential scan method under an applied frequency of 100 Hz. Such plots are usually extrapolated in the form of a straight line to the abscissa, where the resulting slope is used to obtain valuable information regarding the flat band potential (V_{FB}) and nature of charge carrier density (N_A) in a material [58, 59]. In our case, the experiments were carried out through exposing 1 cm² of the electrode material to a standard phosphate based buffer solution (pH 6/7). Figure 6a shows the MS plot for the Cu-In-O/ZnO made p-n heterostructures, where the negative slope was used to estimate the V_{FB} as -0.47 V (SCE). Here, the linear dependence of capacitance values with respect to the applied negative potentials (up to - 0.6 V) illustrates the heterojunction based diode-like behaviour at low operating voltages. The observed trend could also be reasoned with the realization of an abrupt junction in the depletion region at the heterojunction interface [60]. The MS plot for D_1 and D_2 has been additionally discussed in the supplementary information (Figure S8). This

was used to personify the n-type and p-type conductivity in ZnO and Cu-In-O, which possessed a carrier density of around 10^{20} and 10^{18} cm^{-3} , correspondingly.

Figure 6b shows the Nyquist type impedance plots that illustrate the occurrence of two partial semicircles, irrespective of the investigated material system. Here, the one in the high-frequency region corresponds to the charge transfer resistance (R_{ct}) involved in the Faradaic redox process at the electrode/electrolyte interface. The origin of such resistance (associated with the sum of electrolyte and material resistance) could be correlated with the difference in conductivity between the oxide nanocrystals and electrolyte, which further results with a non-uniform continuity in the charge transfer process to take place at electrode/electrolyte interface [61]. Similarly, the second incomplete semicircle observed along the low-frequency region could be attributed to the diffusion of ions across the electrode. To evaluate the value of R_{ct} , the obtained Nyquist plots were fitted with an equivalent circuit, which is shown in the inset of Figure 6a. The detailed procedure involved in the same has been discussed in the supplementary information. The R_{ct} value was estimated to be around 373, 7.85 and 29.87 $\text{k}\Omega$ cm^2 , for D_1 , D_2 and D_3 , respectively. The R_{ct} value for Cu-In-O/ZnO nanowires made heterostructure appears to be apparently much smaller than that of the pristine wires, suggesting the present architecture to effectively promote the interfacial charge transport and photon induced charge carrier separation (upon illumination) [57]. The physical interpretation for rest of the fitted circuit is provided in Table ST1 (ESI) and discussed accordingly.

Finally, we would like to suggest that the observed results clearly dictates the remarkable potential of the investigated systems in enabling us to identify an efficient material for novel functions that include solar cells, sensors, photodetectors and other optoelectronic devices.

Conclusion:

Cu-In-O nanocomposites and p-Cu-In-O/n-ZnO made heterostructures have been successfully realized through a complete solution based strategy. In this regard, the structural characteristics and 15-20 nm scaled particulate-like features of Cu-In-O were studied in detail using XRD, XPS, Raman and electron microscopic tools. The room-temperature emission characteristics of Cu-In-O revealed the occurrence of transitions that spreads across the red and near-IR region of the luminescence spectrum. The nature of charge carriers, carrier density and other electrochemical characteristics of the composite were studied using Mott-Schottky and Nyquist type impedance plots, respectively. The potential of Cu-In-O composite for optoelectronic applications was demonstrated by fabricating a p-n heterostructure composed of p-Cu-In-O/n-ZnO nanowires. The novel architecture/material was found to exhibit a remarkable photoresponse and high absorbance over the UV and entire visible region, signifying their potential to be employed as effective light absorbing materials in heterojunction devices. The investigated architecture also promises an improvement in the diode functionalities and in extending their scope beyond photodiodes for much more exciting and potential applications.

Acknowledgement:

The authors acknowledge the research supported by Leading Foreign Research Institute Recruitment Program, through the National Research Foundation of Korea (NRF) funded by Ministry of Education, Science and Technology (MEST) (No. 2014-039452).

References:

1. R. Nechache, C. Harnagea, S. Li, L. Cardenas, W. Huang, J. Chakrabartty and F. Rosei, *Nat. Photonics*, 2015, **9**, 61-67.

2. Zhe Liu, Jing Xu, Di Chenb and Guozhen Shen, *Chem. Soc. Rev.*, 2015, **44**, 161-192.
3. J. Mannhart and D. G. Schlom, *Science*, 2010, **327**, 1607-1611.
4. H. Y. Hwang, Y. Iwasa, M. Kawasaki, B. Keimer, N. Nagaosa, Y. Tokura, *Nat. Mater.*, 2012, **11**, 103-113.
5. Zhiming Bai, Xiaoqin Yan, Xiang Chen, Yan Cui, Pei Lin, Yanwei Shen and Yue Zhang, *RSC Adv.*, 2013, **3**, 17682.
6. Xi Wang, Wei Tian, Meiyong Liao, Yoshio Bando and Dmitri Goldberg, *Chem. Soc. Rev.*, 2014, **43**, 1400.
7. Beat Buesser and Sotiris E. Pratsinis, *Annu. Rev. Chem. Biomol. Eng.*, 2012, **3**, 103-127.
8. Jian Tian, Zhenhuan Zhao, Anil Kumar, Robert I. Boughton and Hong Liu, *Chem. Soc. Rev.*, 2014, **43**, 6920-6937.
9. S. Rupesh Devan, A. Ranjit Patil, Jin-Han Lin and Yuan-Ron Ma, *Adv. Funct. Mater.*, 2012, **22**, 3326-3370.
10. R. F. P. Martins, A. Ahnood, N. Correia, L. M. N. P. Pereira, R. Barros, P. M. C. B. Barquinha, R. Costa, I. M. M. Ferreira, A. Nathan and E. E. M. C. Fortunato, *Adv. Funct. Mater.*, 2013, **23**, 2153-2161.
11. Meital Segev-Bar and Hossam Haick, *ACS Nano*, 2013, **7**, 8366-8378.
12. Gunuk Wang, Yang Yang, Jae-Hwang Lee, Vera Abramova, Huilong Fei, Gedeng Ruan, Edwin L. Thomas and James M. Tour, *Nano Lett.*, 2014, **14**, 4694-4699.
13. Christophe Avis, Hye Rim Hwang and Jin Jang, *ACS Appl. Mater. Interfaces*, 2014, **6**, 10941-10945.
14. Rachel S. Selinsky, Qi Ding, Matthew S. Faber, John C. Wright and Song Jin, *Chem. Soc. Rev.*, 2013, **42**, 2963-2985.

15. J. Meyer, S. Hamwi, M. Kröger, W. Kowalsky, T. Riedl, and A. Kahn, *Adv. Mater.*, 2012, **24**, 5408-5427.
16. T. Mark Greiner and Zheng-Hong Lu, *NPG Asia Materials*, 2013, **5**, e55.
17. G. Mohan Kumar, V. Raman, J. Kawakita, P. Ilanchezhiyan and R. Jayavel, *Dalton Trans.*, 2010, **39**, 8325-8330.
18. G. Mohan Kumar, D. H. Kim and J. Park, *CrystEngComm*, 2013, **15**, 8195-8201.
19. S. Manna, K. Das and S. K. De, *ACS Appl. Mater. Interfaces*, 2010, **2**, 1536-1542.
20. Yusheng Xia , Xuxin Pu , Jie Liu , Jie Liang , Pujun Liu , Xiaoqing Li and Xibin Yu, *J. Mater. Chem. A*, 2014, **2**, 6796-6800.
21. S. Samantha Wilson, P. Jeffrey Bosco, Yulia Tolstova, O. David Scanlon, W. Graeme Watson and A. Harry Atwater, *Energy Environ. Sci.*, 2014, **7**, 3606-3610.
22. K. P. Musselman, A. Marin, A. Wisnet, C. Scheu, J. L. MacManus-Driscoll, L. Schmidt-Mende, *Adv. Funct. Mater.*, 2011, **21**, 573-582.
23. J. Xu and D. Xue, *J. Phys. Chem. B*, 2005, **109**, 17157-17161.
24. V. Arun Nikam, Arulraj Arulkashmir, Kothandam Krishnamoorthy, A. Amol Kulkarni and B. L. V. Prasad, *Cryst. Growth Des.*, 2014, **14**, 4329-4334.
25. I. Hamberg and C. G. Granquist, *J. Appl. Phys.*, 1986, **60**, R123-R160.
26. T. Tomita, K. Yamashita and Y. Hayafuji, *Appl. Phys. Lett.*, 2005, **87**, 051911.
27. G. Mohan Kumar, A. Madhan Kumar, P. Ilanchezhiyan and T. W. Kang, *Nanoscale*, 2014, **6**, 11226-11231.
28. Chan-Shan Yang, Chan-Ming Chang, Po-Han Chen, Peichen Yu and Ci-Ling Pan, *Opt. Express*, 2013, **21**, 16670-16682.
29. Miriam S. Vitiello, Dominique Coquillat, Leonardo Viti, Daniele Ercolani, Frederic Teppe, Alessandro Pitanti, Fabio Beltram, Lucia Sorba, Wojciech Knap and Alessandro Tredicucci, *Nano Lett.*, 2012, **12**, 96-101.

30. Yumi Ahn, Youngjun Jeong, Donghwa Lee and Youngu Lee, *ACS Nano*, 2015, **9**, 3125–3133.
31. Rahul Sharma; Jin Hwan Kim and Yoon-Bong Hahn, *Sci. Adv. Mater.*, 2012, **4**, 978-984.
32. A. Zainelabdin, S. Zaman, G. Amin, O. Nur and M. Willander, *Appl. Phys. A*, 2012, **108**, 921–928.
33. Babak Nikoobakht, Xudong Wang, Andrew Herzing and Jian Shi, *Chem. Soc. Rev.*, 2013, **42**, 342-365.
34. U. Ozgur, Y. I. Alivov, C. Liu, A. Teke, M.A. Reshchikov, S. Dogan, V. Avrutin, S. J. Cho, H. Morkoç, *J. Appl. Phys.*, 2005, **98**, 041301.
35. C. K. Xu, J. M. Wu, U. V. Desai and D. Gao, *Nano Lett.*, 2012, **12**, 2420-2424.
36. M. Law, L. E. Greene, J. C. Johnson, R. Saykally and P. D. Yang, *Nat. Mater.*, 2005, **4**, 455-459.
37. L. Debbichi, M. C. Marco de Lucas, J. F. Pierson and P. Krüger, *J. Phys. Chem. C*, 2012, **116**, 10232-10237.
38. J. F. Xu, W. Ji, Z. X. Shen, W. S. Li, S. H. Tang, X. R. Ye, D. Z. Jia and X. Q. Xin, *J. Raman Spectrosc.*, 1999, **30**, 413-415.
39. Sourav Ghosh, Mouni Roy and Milan Kanti Naskar, *Cryst. Growth Des.*, 2014, **14**, 2977-2984.
40. G. A. Kourouklis, A. Jayaraman, B. Batlogg, R. J. Cava, M. Stavola, D. M. Krol, E. A. Rietman, and L. F. Schneemeyer, *Phys. Rev. B*, 1987, **36**, 8320-8324.
41. D. Liu, W. W. Lei, B. Zou, S. D. Yu, J. Hao, K. Wang, B. B. Liu, Q. L. Cui and G. T. Zou, *J. Appl. Phys.*, 2008, **104**, 083506.
42. Shaodong Sun, Yuexia Sun, Xiaozhe Zhang, Hongjia Zhang, Xiaoping Song and Zhimao Yang, *CrystEngComm*, 2013, **15**, 5275-5282.

43. Yanbao Zhao, Zhijun Zhang, Zhishen Wu and Hongxin Dang, *Langmuir*, 2004, **20**, 27-29.
44. Davide Barreca, Alberto Gasparotto, Chiara Maccato, Eugenio Tondello, Oleg I. Lebedev and Gustaaf Van Tendeloo, *Cryst. Growth Des.*, 2009, **9**, 2470-2480.
45. J. P. Espinós, J. Morales, A. Barranco, A. Caballero, J. P. Holgado and A. R. González-Elipe, *J. Phys. Chem. B*, 2002, **106**, 6921-6929.
46. J. F. Moulder, W. F. Stickle, P. E. Sobol and K. D. Bomben, in *Handbook of X-ray photoelectron spectroscopy*, ed. by J. Chastain and R. C. King, Jr, (ULVAC-PHI, Inc., Chigasaki, 1995, 72-73.
47. W. T. Yao, S. H. Yu, Y. Zhou, J. Jiang, Q. S. Wu, L. Zhang and J. Jiang, *J. Phys. Chem. B*, 2005, **109**, 14011-14016.
48. Feng Li, Lihong Zhang, David G. Evans and Xue Duan, *Colloids Surf. A*, 2004, **244**, 169-177.
49. F. P. Koffyberg and F. A. Benko, *J. Appl. Phys.*, 1982, **53**, 1173-1177.
50. X. Zhao, P. Wang and B. Li, *Chem. Commun.*, 2010, **46**, 6768-6770.
51. W. U. Dangxin, Z. Qiming and T. Meng, *Phys. Rev. B*, 2006, **73**, 235206.
52. Anagh Bhaumik, Austin M. Shearin, Rishi Patel and Kartik Ghosh, *Phys. Chem. Chem. Phys.*, 2014, **16**, 11054-11066.
53. M. A. M. Jaskari, *Modell. Simul. Mater. Sci. Eng.*, 2006, **14**, 207-216.
54. G. Ramakrishna, K. Ajay Singh, K. Dipak Palit and N. Hirendra Ghosh, *J. Phys. Chem. B*, 2004, **108**, 4775-4783.
55. H. Cao, X. Qiu, Y. Liang, Q. Zhu and M. Zhao, *Appl. Phys. Lett.*, 2003, **83**, 761-763.
56. S. Girish Kumar and K. S. R. Koteswara Rao, *Energy Environ. Sci.*, 2014, **7**, 45-102.

57. Zhuo Kang, Xiaoqin Yan, Yunfei Wang, Zhiming Bai, Yichong Liu, Zheng Zhang, Pei Lin, Xiaohui Zhang, Haoge Yuan, Xueji Zhang and Yue Zhang, *Sci. Rep.*, 2015, **5**, 7882.
58. Chia-Ying Chiang, Yoon Shin and Sheryl Ehrman, *J. Electrochem. Soc.*, 2012, **159**, B227-B231.
59. H. Liu, G. Piret, B. Sieber, J. Laureyns, P. Roussel, W. Xu, R. Boukherroub and S. Szunerits, *Electrochem. Commun.*, 2009, **11**, 945– 949.
60. Kwang-Ki Baek and L. Harry Tuller, *Solid State Ionics*, 1995, **75**, 179-186.
61. Sumanta Kumar Meher, P. Justin and G. Ranga Rao, *ACS Appl. Mater. Interfaces*, 2011, **3**, 2063-2073.

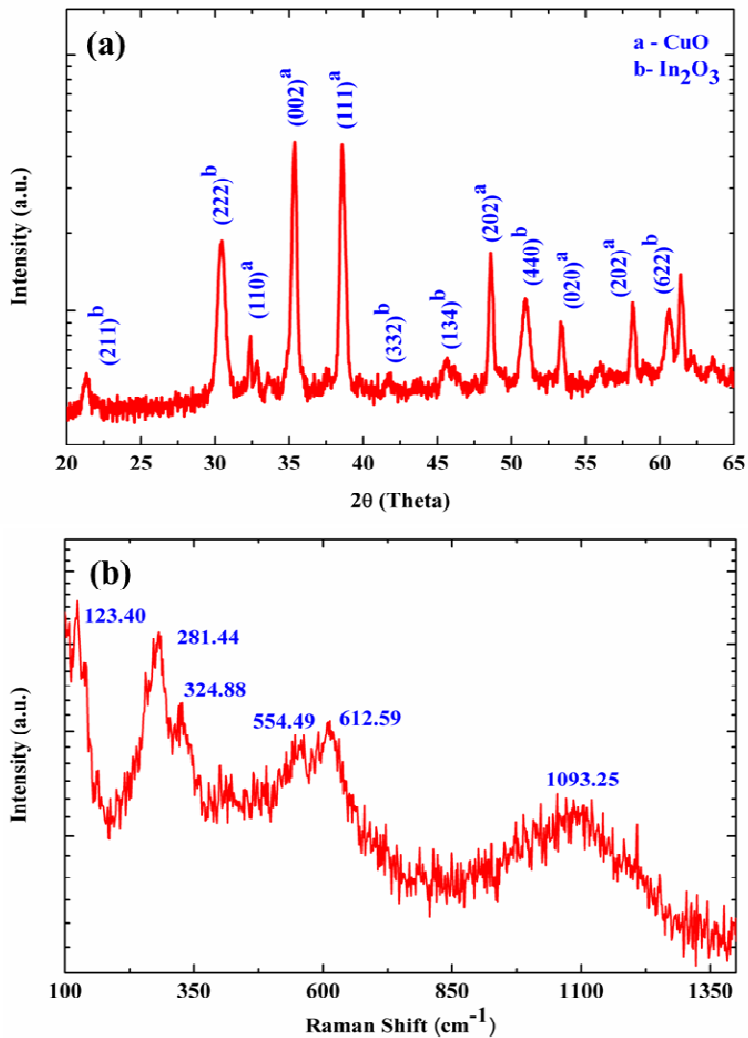


Figure 1: (a) XRD pattern revealing the mutual existence of CuO and In_2O_3 characteristics in solution processed Cu-In-O nanocomposites that were annealed at 800°C . (b) Room-temperature Raman spectrum revealing the enhanced activity of IR modes in Cu-In-O through the satellite structure at 554 cm^{-1} .

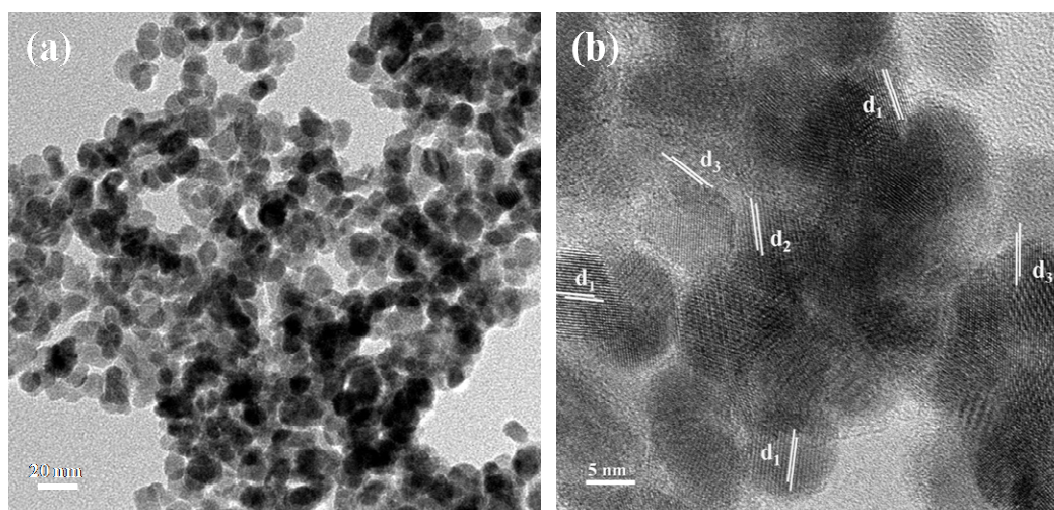


Figure 2: (a) TEM suggests the morphological identities between CuO and In_2O_3 to be similar in Cu-In-O. (b) HRTEM illustrates the d spacing values corresponding to that of monoclinic phased CuO (d_1 {002} and d_2 {111}) and cubic phased In_2O_3 (d_3 {222}) in Cu-In-O.

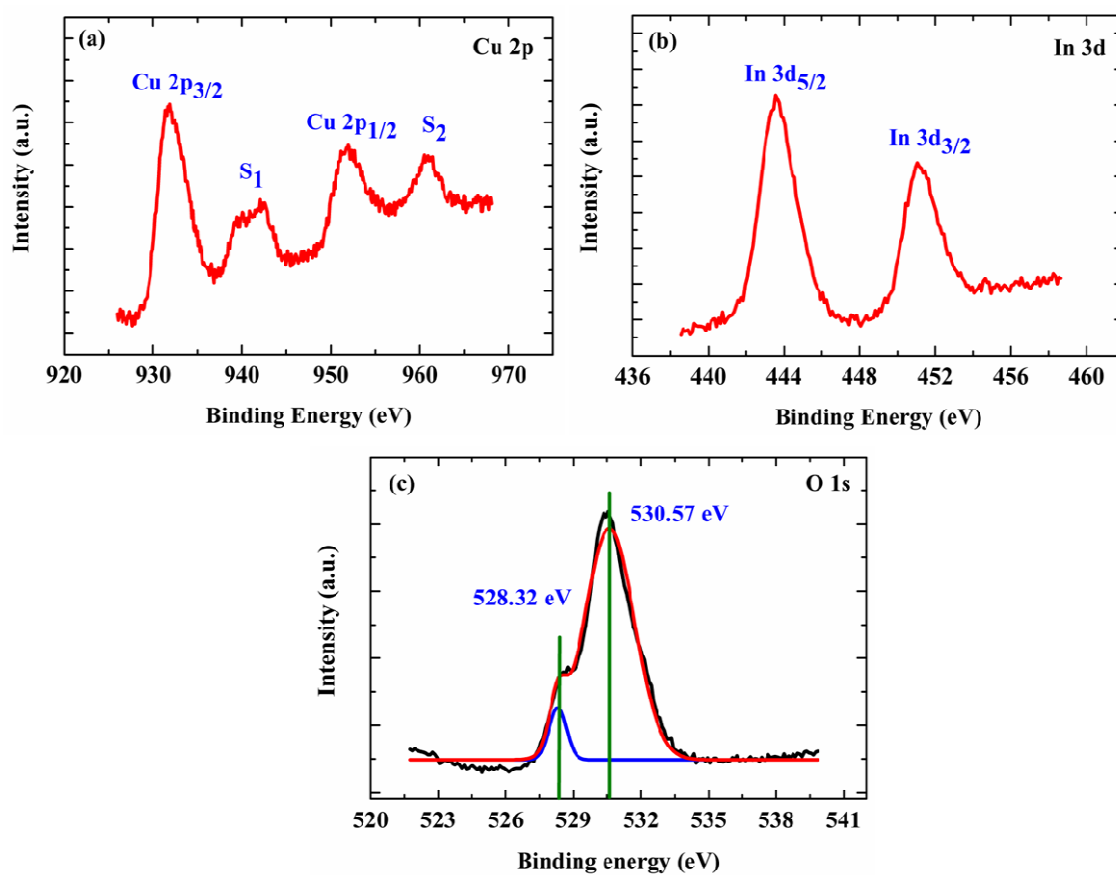


Figure 3: X-ray photoelectron spectroscopic results corresponding to (a) Cu 2p, (b) In 3d and (c) O 1s core levels that suggest the 2+ and 3+ state of Cu and In in Cu-In-O.

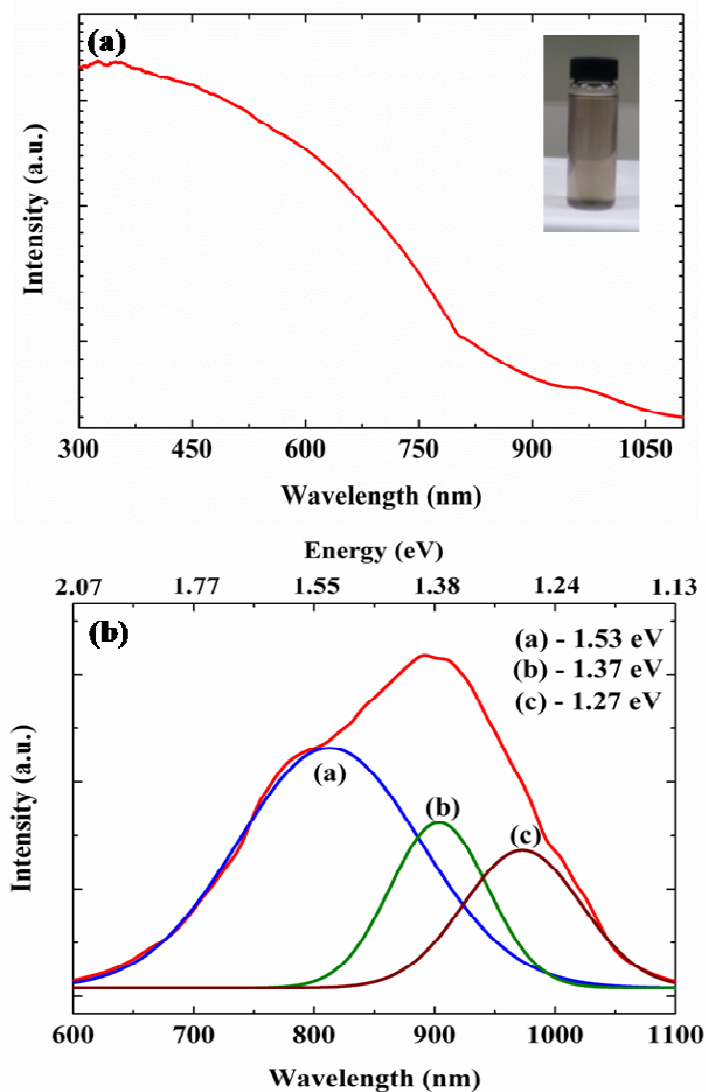


Figure 4: (a) UV-vis absorbance spectrum corresponding to the Cu-In-O colloidal dispersion (inset of 4a) that was involved in the fabrication of p-n heterostructures. The spectrum reveals the potential of composite to absorb light across the UV and visible spectrum, respectively (b) Photoluminescence spectrum of Cu-In-O composites (at an excitation wavelength of 488 nm) along with its corresponding resolved spectra, where the enhanced optical activity of the

composites could be observed along the red and near-infrared region of electromagnetic spectrum.

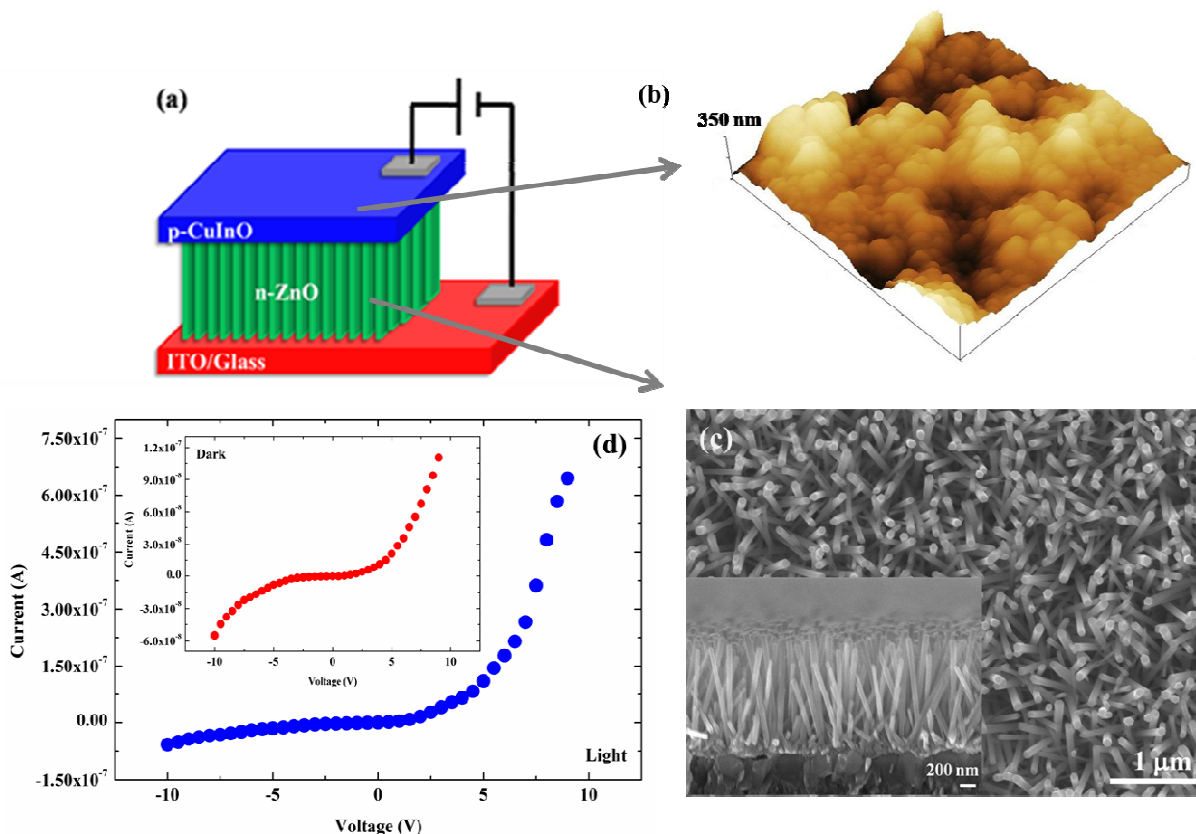
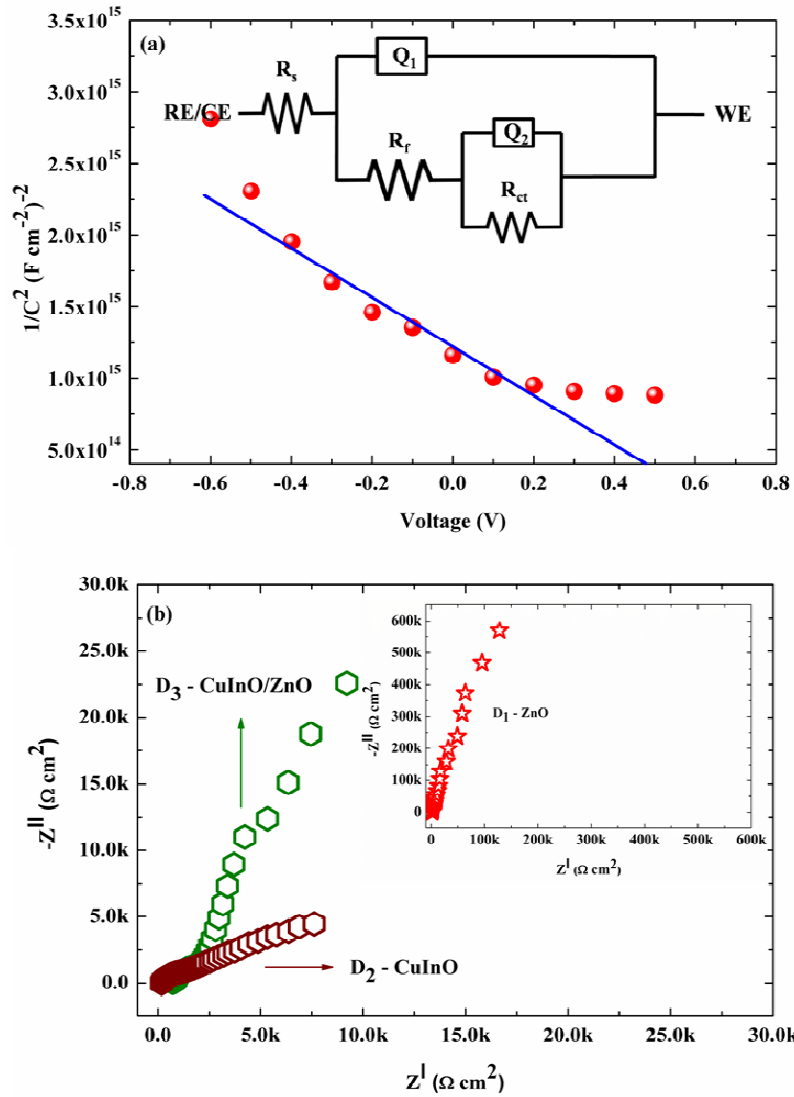


Figure 5: (a) Schematic representation of solution processed p-Cu-In-O/n-ZnO nanowire made heterostructures. (b) AFM image on a $2 \times 2 \mu\text{m}$ scale revealing the Cu-In-O crystals to be well adhered as agglomerates on the surface of ZnO nanowires. The interface between Cu-In-O/ZnO was also investigated through a scanning electron microscope, whose results are shown in Figure S4 (ESI). (c) Surface and cross-sectional representation of ZnO

nanowires

I-V

on ITO. (d)



characteristics that illustrate the improved photoelectronic behaviour under illuminated conditions.

Figure 6: (a) Mott-Schottky plot signifying the negative slope in Cu-In-O/ZnO made heterostructures and a V_{FB} of -0.47 V at an applied frequency of 100 Hz. (b) Nyquist type impedance plots for pristine ZnO nanowires (D_1), Cu-In-O deposits (D_2) and Cu-In-O/ZnO made heterostructures (D_3), with the corresponding equivalent circuit at the inset of (a). The n- and p-type characteristics corresponding to D_1 and D_2 and their carrier density and V_{FB} were determined using their MS plots shown in Figure S8 (ESI).